One-prong τ decays with kaons

The ALEPH Collaboration

R. Barate, D. Decamp, P. Ghez, C. Goy, J.-P. Lees, E. Merle, M.-N. Minard, B. Pietrzyk
Laboratoire de Physique des Particules (LAPP), IN[2]P[3]-CNRS, F-74019 Annecy-le-Vieux Cedex, France

R. Alemany, M.P. Casado, M. Chmeissani, J.M. Crespo, E. Fernandez, M. Fernandez-Bosman, Ll. Garrido,[15]
E. Graugès, A. Juste, M. Martinez, G. Merino, R. Miquel, Ll.M. Mir, A. Pacheco, I.C. Park, I. Riu
Institut de Física d'Altes Energies, Universitat Autònoma de Barcelona, E-08193 Bellaterra (Barcelona), Spain[7]

A. Colaleo, D. Creanza, M. de Palma, G. Gelao, G. Iaselli, G. Maggi, M. Maggi, S. Nuzzo, A. Ranieri, G. Raso,
F. Ruggieri, G. Selvaggi, L. Silvestris, P. Tempesta, A. Tricomi,[3] G. Zito
Dipartimento di Fisica, INFN Sezione di Bari, I-70126 Bari, Italy

X. Huang, J. Lin, Q. Ouyang, T. Wang, Y. Xie, R. Xu, S. Xue, J. Zhang, L. Zhang, W. Zhao
Institute of High-Energy Physics, Academia Sinica, Beijing, P.R. China[8]

D. Abbaneo, U. Becker,[19] G. Boix,[6] M. Cattaneo, V. Ciulli, G. Dissertori, H. Drevermann, R.W. Forty, M. Frank,
A.W. Halley, J.B. Hansen, J. Harvey, P. Janot, B. Jost, I. Lehraus, O. Leroy, P. Mato, A. Minten, A. Moutoussi,
F. Ranjard, L. Rolandi, D. Rousseau, D. Schlatter, M. Schmitt,[20] O. Schneider,[23] W. Tejessy, F. Teubert,
I.R. Tomalin, E. Tournefier, A.E. Wright
European Laboratory for Particle Physics (CERN), CH-1211 Geneva 23, Switzerland

Z. Ajaltouni, F. Badaud, G. Chazelle, O. Deschamps, A. Falvard, C. Ferdi, P. Gay, C. Guicheney, P. Henrard,
J. Jousset, B. Michel, S. Monteil, J-C. Montret, D. Pallin, P. Perret, F. Podlyski
Laboratoire de Physique Corpusculaire, Université Blaise Pascal, IN[2]P[3]-CNRS, Clermont-Ferrand, F-63177 Aubière, France

J.D. Hansen, J.R. Hansen, P.H. Hansen, B.S. Nilsson, B. Rensch, A. Wäänänen
Niels Bohr Institute, DK-2100 Copenhagen, Denmark[9]

G. Daskalakis, A. Kyriakis, C. Markou, E. Simopoulou, I. Siotis, A. Vayaki
Nuclear Research Center Demokritos (NRCD), GR-15310 Attiki, Greece

A. Blondel, G. Bonneaud, J.-C. Brient, A. Rougé, M. Rumpf, M. Swynghedauw, M. Verderi, H. Videau
Laboratoire de Physique Nucléaire et des Hautes Energies, Ecole Polytechnique, IN[2]P[3]-CNRS, F-91128 Palaiseau Cedex, France

E. Focardi, G. Parrini, K. Zachariadou
Dipartimento di Fisica, Università di Firenze, INFN Sezione di Firenze, I-50125 Firenze, Italy

R. Cavanaugh, M. Corden, C. Georgiopoulos
Supercomputer Computations Research Institute, Florida State University, Tallahassee, FL 32306-4052, USA [13,14]

A. Antonelli, G. Bencivenni, G. Bologna,[4] F. Bossi, P. Campana, G. Capon, F. Cerutti, V. Chiarella, P. Laurelli,
G. Mannocchi,[5] F. Murtas, G.P. Murtas, L. Passalacqua, M. Pepe-Altarelli[1]
Laboratori Nazionali dell'INFN (LNF-INFN), I-00044 Frascati, Italy

L. Curtis, J.G. Lynch, P. Negus, V. O'Shea, C. Raine, P. Teixeira-Dias, A.S. Thompson
Department of Physics and Astronomy, University of Glasgow, Glasgow G12 8QQ, UK[10]

O. Buchmüller, S. Dhamotharan, C. Geweniger, P. Hanke, G. Hansper, V. Hepp, E.E. Kluge, A. Putzer, J. Sommer,
K. Tittel, S. Werner,[19] M. Wunsch
Institut für Hochenergiephysik, Universität Heidelberg, D-69120 Heidelberg, Germany[16]

R. Beuselinck, D.M. Binnie, W. Cameron, P.J. Dornan,[1] M. Girone, S. Goodsir, E.B. Martin, N. Marinelli,
J.K. Sedgbeer, P. Spagnolo, E. Thomson, M.D. Williams
Department of Physics, Imperial College, London SW7 2BZ, UK[10]

V.M. Ghete, P. Girtler, E. Kneringer, D. Kuhn, G. Rudolph
Institut für Experimentalphysik, Universität Innsbruck, A-6020 Innsbruck, Austria[18]

A.P. Betteridge, C.K. Bowdery, P.G. Buck, P. Colrain, G. Crawford, A.J. Finch, F. Foster, G. Hughes, R.W.L. Jones,
N.A. Robertson, M.I. Williams
Department of Physics, University of Lancaster, Lancaster LA1 4YB, UK[10]

I. Giehl, C. Hoffmann, K. Jakobs, K. Kleinknecht, G. Quast, B. Renk, E. Rohne, H.-G. Sander, P. van Gemmeren,
H. Wachsmuth, C. Zeitnitz
Institut für Physik, Universität Mainz, D-55099 Mainz, Germany[16]

J.J. Aubert, C. Benchouk, A. Bonissent, J. Carr,[1] P. Coyle, F. Etienne, F. Motsch, P. Payre, M. Talby, M. Thulasidas
Centre de Physique des Particules, Faculté des Sciences de Luminy, IN^{2}P^3-CNRS, F-13288 Marseille, France

M. Aleppo, M. Antonelli, F. Ragusa
Dipartimento di Fisica, Università di Milano e INFN Sezione di Milano, I-20133 Milano, Italy

R. Berlich, V. Büscher, H. Dietl, G. Ganis, K. Hüttmann, G. Lütjens, C. Mannert, W. Männer, H.-G. Moser,
S. Schael, R. Settles, H. Seywerd, H. Stenzel, W. Wiedenmann, G. Wolf
Max-Planck-Institut für Physik, Werner-Heisenberg-Institut, D-80805 München, Germany[p]

P. Azzurri, J. Boucrot, O. Callot, S. Chen, A. Cordier, M. Davier, L. Duflot, J.-F. Grivaz, Ph. Heusse, A. Höcker,
A. Jacholkowska, D.W. Kim,[12] F. Le Diberder, J. Lefrançois, A.-M. Lutz, M.-H. Schune, J.-J. Veillet, I. Videau,[1]
D. Zerwas
Laboratoire de l'Accélérateur Linéaire, Université de Paris-Sud, IN^{2}P^3-CNRS, F-91898 Orsay Cedex, France

G. Bagliesi, S. Bettarini, T. Boccali, C. Bozzi,[24] G. Calderini, R. Dell'Orso, I. Ferrante, L. Foà, A. Giassi, A. Gregorio,
F. Ligabue, A. Lusiani, P.S. Marrocchesi, A. Messineo, F. Palla, G. Rizzo, G. Sanguinetti, A. Sciabà, G. Sguazzoni,
R. Tenchini, C. Vannini, A. Venturi, P.G. Verdini
Dipartimento di Fisica dell'Università, INFN Sezione di Pisa, e Scuola Normale Superiore, I-56010 Pisa, Italy

G.A. Blair, G. Cowan, M.G. Green, T. Medcalf, J.A. Strong, J.H. von Wimmersperg-Toeller
Department of Physics, Royal Holloway & Bedford New College, University of London, Surrey TW20 OEX, UK[10]

D.R. Botterill, R.W. Clifft, T.R. Edgecock, P.R. Norton, J.C. Thompson
Particle Physics Dept., Rutherford Appleton Laboratory, Chilton, Didcot, Oxon OX11 OQX, UK[10]

B. Bloch-Devaux, P. Colas, S. Emery, W. Kozanecki, E. Lançon, M.-C. Lemaire, E. Locci, P. Perez, J. Rander,
J.-F. Renardy, A. Roussarie, J.-P. Schuller, J. Schwindling, A. Trabelsi,[21] B. Vallage
CEA, DAPNIA/Service de Physique des Particules, CE-Saclay, F-91191 Gif-sur-Yvette Cedex, France[17]

S.N. Black, J.H. Dann, R.P. Johnson, H.Y. Kim, N. Konstantinidis, A.M. Litke, M.A. McNeil, G. Taylor
Institute for Particle Physics, University of California at Santa Cruz, Santa Cruz, CA 95064, USA[22]

C.N. Booth, S. Cartwright, F. Combley, M.S. Kelly, M. Lehto, L.F. Thompson
Department of Physics, University of Sheffield, Sheffield S3 7RH, UK[10]

K. Affholderbach, A. Böhrer, S. Brandt, C. Grupen, G. Prange
Fachbereich Physik, Universität Siegen, D-57068 Siegen, Germany[16]

G. Giannini, B. Gobbo
Dipartimento di Fisica, Università di Trieste e INFN Sezione di Trieste, I-34127 Trieste, Italy

J. Rothberg, S. Wasserbaech
Experimental Elementary Particle Physics, University of Washington, WA 98195 Seattle, USA

S.R. Armstrong, E. Charles, P. Elmer, D.P.S. Ferguson, Y. Gao, S. González, T.C. Greening, O.J. Hayes, H. Hu,
S. Jin, P.A. McNamara III, J.M. Nachtman,[2] J. Nielsen, W. Orejudos, Y.B. Pan, Y. Saadi, I.J. Scott, J. Walsh,
Sau Lan Wu, X. Wu, G. Zobernig
Department of Physics, University of Wisconsin, Madison, WI 53706, USA[11]

Abstract. One-prong τ decays into final states involving kaons are studied with about $161\,000$ $\tau^+\tau^-$ events collected by the ALEPH detector from 1991 to 1995. Charged kaons are identified by dE/dx measurement, while K_L^0's are detected through their interaction in calorimeters. Branching ratios are measured for the inclusive mode, $B(\tau^- \to K^- X \nu_\tau) = (1.52 \pm 0.04 \pm 0.04)\%$, where X can be any system of neutral particles, and for the exclusive modes

$$
\begin{aligned}
B(\tau^- \to K^- \nu_\tau) &= (6.96 \pm 0.25 \pm 0.14) \times 10^{-3}, \\
B(\tau^- \to K^- \pi^0 \nu_\tau) &= (4.44 \pm 0.26 \pm 0.24) \times 10^{-3}, \\
B(\tau^- \to K^- \pi^0 \pi^0 \nu_\tau) &= (0.56 \pm 0.20 \pm 0.15) \times 10^{-3}, \\
B(\tau^- \to K^- \pi^0 \pi^0 \pi^0 \nu_\tau) &= (0.37 \pm 0.21 \pm 0.11) \times 10^{-3}, \\
B(\tau^- \to K^- K^0 \nu_\tau) &= (1.62 \pm 0.21 \pm 0.11) \times 10^{-3}, \\
B(\tau^- \to K^- K^0 \pi^0 \nu_\tau) &= (1.43 \pm 0.25 \pm 0.15) \times 10^{-3}, \\
B(\tau^- \to \overline{K^0} \pi^- \nu_\tau) &= (9.28 \pm 0.45 \pm 0.34) \times 10^{-3}, \\
B(\tau^- \to \overline{K^0} \pi^- \pi^0 \nu_\tau) &= (3.47 \pm 0.53 \pm 0.37) \times 10^{-3},
\end{aligned}
$$

where the first error is statistical and the second is systematical. Upper limits for $B(\tau^- \to \overline{K^0} \pi^- \pi^0 \pi^0 \nu_\tau)$ and $B(\tau^- \to K^- K^0 \pi^0 \pi^0 \nu_\tau)$ are also obtained. Mass spectra in the final states are investigated in order to study the relevant dynamics.

1 Introduction

The study of τ decays involving kaons is necessary in order to understand the strange hadronic τ sector as such, but also to provide a better control over nonstrange decay modes. Both issues play an important role in the low energy QCD analyses accessible through hadronic τ decays.

Results on charged kaons in three-prong decays [1] and on K_S^0 production [2] have already been published. In this paper, one-prong decays are investigated. Taking advantage of their simpler topology, the analysis combines the dE/dx measurement of the charged track and the reconstruction of K_L^0's through their hadronic showers.

The first analysis of one-prong final states with a charged kaon was presented using $38\,000$ selected $\tau^+\tau^-$ events collected in 1991 and 1992 [3], and an update was given adding the 1993 data for a total of $64\,000$ selected $\tau^+\tau^-$ events [4], enabling the study of the inclusive kaon mode and the three exclusive channels[1] $K^-\nu_\tau$, $K^-\pi^0\nu_\tau$, and $K^-\pi^0\pi^0\nu_\tau$. Analyses with K_L^0 detection were published with the same data sets [4,5]. In this paper, final results are given using the full LEP1 statistics corresponding to 161k selected $\tau^+\tau^-$ events. Several improvements are implemented, increasing selection efficiencies and reducing systematic uncertainties. This is achieved through a better use of all the available calorimetric information, imbedded into a more efficient method for measuring the K_L^0 signal. Because of the larger statistics, a better understanding of the systematic effects is also acquired. The present results therefore supersede those from previous analyses on one-prong kaon modes [3–5].

After a short description of the ALEPH detector and the event selection, the dE/dx calibration using muons is presented in detail. Then, the calorimetric method for

[1] Throughout this paper, charge conjugate states are implied

K^0_L detection, taking advantage of the granularity of the calorimeters and the special τ decay kinematics, is described. Branching ratios for inclusive charged kaon production and exclusive channels involving charged and neutral kaons are derived through statistical methods, both for dE/dx and calorimetry. A detailed account of the systematic uncertainties is given next, showing that in all cases the measurements are still statistically limited. Finally, the underlying dynamics in these decays is addressed through the study of invariant mass spectra for exclusive decay samples.

2 The ALEPH detector

A detailed description of the ALEPH detector can be found elsewhere [6]. Here only the most relevant features for this analysis are described.

The momenta of the charged tracks are measured by means of a central tracking system consisting of a silicon microstrip vertex detector, an inner tracking chamber (ITC), and a time projection chamber (TPC). All of these three tracking devices are immersed in a 1.5 T axial magnetic field, and achieve a transverse momentum resolution for the charged track of $\sigma_{p_t}/p_t = 6 \times 10^{-4} p_t \oplus 0.005$, with p_t in GeV/c.

Two subdetectors, the electromagnetic calorimeter (ECAL) and the hadron calorimeter (HCAL), produce the energy measurement for electrons and hadrons. The ECAL consists of 45 layers of sandwiched lead sheets and proportional wire chambers, representing 22 radiation lengths, and is used to measure the energy deposit of electrons and photons. Its fine granularity is essential to the reconstruction of π^0's, and the longitudinal segmentation with three stacks measures the electromagnetic profile of the detected shower. The energy resolution in the ECAL is measured to be $\sigma_E/E = 0.18/\sqrt{E(\text{GeV})} + 0.09$. Hadronic energy is measured by the HCAL, which is composed of a 1.2 m thick iron stack serving as the yoke for magnetic flux return. Streamer tubes are inserted into the gaps of the iron stacks, giving 23 energy samples. The energy resolution of the HCAL for pions at normal incidence is $\sigma_E/E = 0.85/\sqrt{E(\text{GeV})}$. Outside the HCAL, two layers of streamer tubes are used to complete the muon detection.

In the data sample used for this analysis, all components of the detector are required to be operational. Furthermore, one of the following trigger conditions is required: a minimum ECAL energy of 6 GeV, or a track segment in the ITC pointing to an energy deposit in the ECAL of at least 1.2 GeV, or a track segment matching the signal of a penetrating particle in the HCAL. By comparing redundant and independent triggers involving the tracking detectors and the main calorimeters, the trigger efficiency for τ pair events is estimated to be better than 99.99% within the selection criteria used in this analysis.

The measurement of the ionization dE/dx deposited by the charged particles when traversing the TPC volume is the only tool in ALEPH for the identification of charged

hadrons. Ideally, the dE/dx ionization can be measured with up to 338 samples. However, in some cases a charged track may not have such a number of samples because of the following factors: the cracks between the TPC sectors, the geometrically available track length and the applied truncation for avoiding the large fluctuations caused by δ rays. A minimum of 40 samples is required to ensure a good particle identification, rejecting about 0.1% of the events.

3 Event selection

A sample of about 161 000 events is obtained using a general τ-pair selection procedure [4,7], from about 202 000 produced τ pairs. The one-prong decays are selected from this sample.

Each event is first divided into two hemispheres separated by the plane perpendicular to the thrust axis of the event. A one-prong hemisphere is required to contain exactly one good charged track, satisfying a minimum of four associated hits in the TPC, an impact parameter in the plane transverse to the beam axis $|d_0| \leq 2$ cm and the distance from the interaction point along the beam axis $|z_0| \leq 10$ cm. Also, the track momentum is required to be larger than 100 MeV/c. To reduce the number of fake K^0_L's produced by additional tracks, each hemisphere candidate is not allowed to contain any unselected charged track associated with at least three hits either in the TPC or the ITC, $|d_0| \leq 20$ cm, $|z_0| \leq 40$ cm and a momentum more than 2 GeV/c. Finally, to identify electrons, muons and hadrons in the one-prong τ candidates, a particle identification [7] is performed, except for the tracks with momenta below 2 GeV/c (where only electrons are identified through their dE/dx) or going through a crack between ECAL modules. All these requirements select a total sample of 143 319 one-prong hadronic τ decays. Hemispheres containing a track with momentum less than 2 GeV/c and not identified as an electron by dE/dx are kept for the K^0_L search performed in Sect. 7.

Then, all selected one-prong candidates are classified according to the number of associated π^0's, which are identified using a photon and π^0 reconstruction algorithm [4]. In this analysis, a π^0 is defined as follows. A resolved π^0 is formed by a pair of photons with an invariant mass consistent with that of a π^0. Photons from high energy π^0's may give rise to electromagnetic showers so close to each other that they cannot be recognized as two separate objects, leading to an unresolved π^0 which is identified by the energy-weighted moment technique [4]. The remaining photons inside a cone of 30° around the thrust axis are called residual photons. They arise from the loss of the partner photons because either of the ECAL energy threshold, the presence of cracks between modules or the overlap with other showers. The residual photons are not used in this analysis. Under these definitions, one-prong τ decays are separated into h^- ($h = \pi$ or K), $h^-\pi^0$, $h^-\pi^0\pi^0$, $h^-\pi^0\pi^0\pi^0$ and the rest (containing one or several residual photons), corresponding to 47 543, 54 171, 10 325, 959 and 30 321 decays, respectively.

Finally, to evaluate the efficiencies and the background contamination, 1.0 million $\tau^+\tau^-$ Monte Carlo events and 5.8 million $q\bar{q}$ are produced by the standard KORALZ [8] and the JETSET 7.4 [9] generators, respectively, with a complete ALEPH detector simulation.

4 dE/dx calibration and probability functions

The ionization energy deposit R is measured in the TPC. The expected R_i and its standard deviation σ_i for a given particle type hypothesis i are initially calculated using a parametrization of the Bethe-Bloch formula fitted to hadronic events [6], in which the environment is rather different from that of the one-prong τ decay where no track overlap occurs. In one-prong hadronic τ decays, the environment is similar to that of the muons from $Z \to \mu^+\mu^-$ or $\tau^- \to \mu^-\bar{\nu}_\mu\nu_\tau$ which provide a pure sample of isolated muon tracks covering the full momentum range and characterized by the same angular distribution in the detector as the hadron sample under study. Therefore, a special and accurate dE/dx calibration can be performed in order to achieve a more precise measurement on the small kaon fraction in τ decays.

The main philosophy of dE/dx calibration follows [3]. Some modifications are made, taking into account slight variations in each period of data taking and allowing for possible small differences between muons and hadrons, due to interactions for the latter.

The calibration is based on a sample of muons selected from $Z \to \mu^+\mu^-$ and $\tau^- \to \mu^-\bar{\nu}_\mu\nu_\tau$, corresponding to 278 079 and 49 620 tracks respectively. Distributions of the variable $x_\mu = \frac{R-R_\mu}{\sigma_\mu}$ are studied as functions of (i) the period of data acquisition; (ii) the polar angle of the track; (iii) the number of dE/dx samples; and (iv) the R value. The calibration gives the new values for R_μ and σ_μ according to

$$R_\mu^{new} = R_\mu^{old} + \bar{x}_\mu^{old} \times \sigma_\mu^{old} \qquad (1)$$

and

$$\sigma_\mu^{new} = \sigma_{x_\mu^{old}} \times \sigma_\mu^{old}, \qquad (2)$$

where $\bar{x}_\mu^{old}$ and $\sigma_{x_\mu^{old}}$ represent the mean and the standard deviation of the initial x_μ distribution. The calibration is performed in an iterative way correcting most of the correlations among the above four factors. The distribution of the calibrated x_μ for the muon sample is parametrized by an initially energy-independent four-Gaussian function $F_\mu(x)$ showing a slight asymmetry. There is still a tiny contamination from residual kaons and pions in the selected muon sample from τ's because of either hadron misidentification as muon or decay in flight. These backgrounds are estimated directly from the Monte Carlo simulation, and the corresponding fractions are fixed in the fit. The final result of the parametrization to the muon sample is shown in Fig. 1, indicating an excellent fit with $\chi^2/ndf = 42.9/46$.

The energy independence of $F_\mu(x)$ is not well satisfied at low momentum, as demonstrated with a large statistics sample of $\gamma\gamma \to \mu^+\mu^-$ events. It is observed that, in the
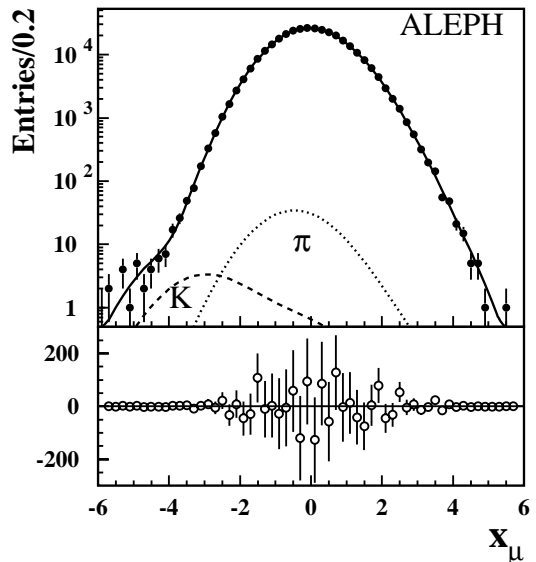
Fig. 1. x_μ distribution for the muon sample (top). The fit is indicated by the solid curve, and the expected residual kaons and pions are shown by dashed and dotted curves, respectively. The residuals between the data and the fit are shown in the bottom plot
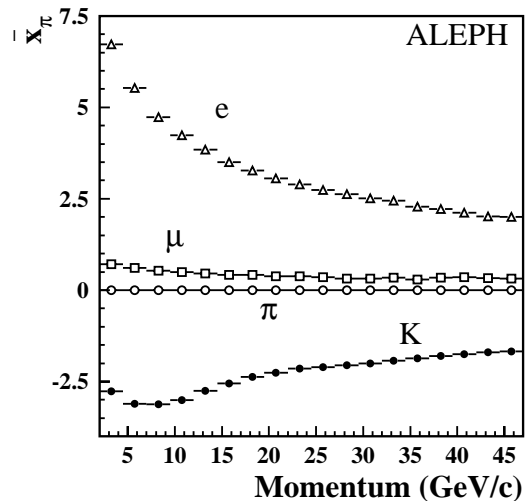
Fig. 2. Separation from pions in standard deviations ($\bar{x}_\pi$) for different particle types as a function of momentum

region below 7 GeV/c, the function becomes more symmetric. This small effect is taken into account in the final parametrization of the resolution function.

Finally, it is assumed that the $x_h(h)$ distribution has the same functional form as that of the muons, namely

$$F_h(x_h) = F_\mu(x_\mu). \qquad (3)$$

With this function, the expected dE/dx response can be generated for any particle type, resulting in a distribution from kaons in terms of x_π of the form

$$G_K(x_\pi) = \frac{\sigma_\pi}{\sigma_K} F_K \left(\frac{x_\pi \sigma_\pi + R_\pi - R_K}{\sigma_K} \right). \qquad (4)$$

The final particle separations in standard deviations are illustrated as a function of momentum in Fig. 2.

5 Calorimetric calibration

Since the K_L^0 component is extracted from the calorimetric response by means of a statistical technique, a calibration of the measurements in both the ECAL and the HCAL is necessary. The details of the calorimetric calibration are described below.

5.1 Definition
of the discriminating variables $\delta\phi$ and δ_E

At LEP energies, the produced τ leptons are strongly Lorentz-boosted with only a few degrees opening angle between any two particles in the final state. However, the bending due to the magnetic field provides an opportunity for separating the calorimetric clusters associated to the K_L^0 and the charged hadron in the HCAL, by making use of the transverse angular offset

$$\delta\phi = \pm|\phi_{barycentre} - \phi_{track\ impact}|, \qquad (5)$$

where the positive sign is taken if the azimuthal angle $\phi_{barycentre}$, determined by the barycentre of energy measured in the HCAL, is inside the bending trajectory of the charged hadron, and the negative sign is taken otherwise; $\phi_{track\ impact}$ is defined as the azimuthal angle for the position of the charged track at the inner radius of the HCAL. The minimum transverse momentum needed for a charged particle to reach the HCAL is about 0.7 GeV/c provided that no energy is lost in the ECAL. K_L^0's from τ decay are emitted at small angle with respect to the charged hadrons, leading to a characteristic negative value of $\delta\phi$ in most of the cases. Throughout this paper $\delta\phi$ is expressed in degrees.

In addition, the K_L^0 signal can be enhanced by exploiting the hadronic energy excess in the calorimeters, measured by the quantity

$$\delta_E = \frac{E - (E_{\pi^0}) - P_h}{C\sqrt{P_h}}, \qquad (6)$$

where E is the sum of the energies measured by both the ECAL and the HCAL in the studied hemisphere, E_{π^0} is the total π^0 energy measured by the ECAL in $h\pi^0(\pi^0)$ modes, P_h is the charged track momentum, the denominator is close to the actual resolution of the calorimeters for hadrons, and $C = 0.9$ (GeV/c)$^{\frac{1}{2}}$. Since K_L^0's from τ decay have a momentum in excess of 3.5 GeV/c, a positive value of δ_E is expected. This procedure differs from the previous analyses [3,4], which used the energy deposit in the HCAL only. In fact more than 50% of K_L^0's interact inside the ECAL and leave part of their energy mostly in the last two stacks, with longitudinal and transverse
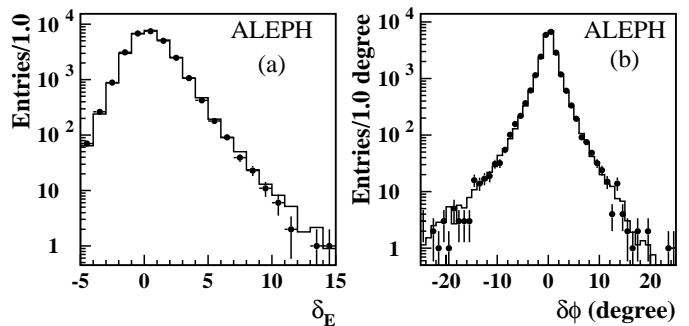
Fig. 3. a The calibrated δ_E distributions for hemispheres with a positive $\delta\phi$. **b** The calibrated $\delta\phi$ distributions for hemispheres with a negative δ_E. Data and Monte Carlo simulation are shown in dots with error bars and in histograms, respectively

profiles different from those of a photon shower. Since the simulation of the relative energy deposits in the ECAL and the HCAL is rather delicate, it is more reasonable to combine the two pieces of information, in order to reduce systematic uncertainties.

In the following, cuts on $\delta\phi$ and δ_E are used separately in order to select samples for calibration.

5.2 Calibration for the energy measurement

Decays with $\delta\phi > 0$, consisting of single charged hadrons with a very small contamination from K_L^0 and unreconstructed π^0, are used for the energy calibration. The total hadronic energy measured by the calorimeters is summed with a 1.3 weight factor for the ECAL, taking into account the ratio of the electromagnetic calorimeter responses to electrons and pions [6]. The calibration provides corrections as a function of the data-taking period and the polar angle, the latter corresponding to varying effective interaction length and geometry of the calorimeters. The same procedure is performed on the Monte Carlo sample so that its δ_E distribution matches data.

The calibration procedures are applied separately for the h, $h\pi^0$ and $h\pi^0\pi^0$ samples. Figure 3a shows a good agreement between data and Monte Carlo simulation in the calibrated δ_E distributions for all the modes. The above calibration is applied to all events, assuming that events with a negative $\delta\phi$ follow the same variation as those with a positive $\delta\phi$.

5.3 Calibration for the barycentre offset $\delta\phi$
in the HCAL

At this stage, a non-K_L^0 sample is selected by requiring hemispheres with a negative sign of δ_E. The $\delta\phi$ distribution is checked and found to be consistent within different periods of data acquisition. For all hadronic samples, the Monte Carlo simulation is in good agreement with data for the $\delta\phi$ mean, but produces a somewhat larger width. This effect is proportional to the energy deposited in the

HCAL, and is used as a correction to the width of the $\delta\phi$ distribution as a function of energy in the Monte Carlo simulation. Figure 3b shows that for the calibrated $\delta\phi$ distribution in the h mode, Monte Carlo simulation is observed to agree with data. The same calibration is applied to the events with a positive δ_E.

6 Channels involving charged kaons

In this section, the inclusive one-prong τ decay is first investigated to finalize the dE/dx calibration, and a measurement of the corresponding kaon fractions is presented. The dE/dx measurement is also exploited to study the exclusive one-prong τ decays, which are classified into K_L^0-reduced and K_L^0-enriched samples. Branching ratios are measured for all the exclusive modes K^-, $K^-\pi^0$, $K^-\pi^0\pi^0$, $K^-\pi^0\pi^0\pi^0$, K^-K^0, $K^-K^0\pi^0$ and $K^-K^0\pi^0\pi^0$.

6.1 Charged kaon fraction in the inclusive mode

To be insensitive to the *a priori* unknown dynamics, the fit to the x_π distribution is performed in momentum slices. Small contaminations from residual muons and electrons are included in the fit, with fractions estimated by the simulation. Beyond calibration (obtained with data), the K/π separation, varying with momentum as shown in Fig. 2, is determined by Monte Carlo (to take into account the kaon and pion momentum distribution in the given slice) and kept fixed in the fit. The $x_\pi(\pi)$ parameters and the kaon fraction are free to vary. Table 1 lists the fit results in the different momentum slices. Figures 4 and 5 show the sum of the fits to x_π for all momentum slices and the kaon yield as a function of momentum for both data and simulation.

Due to the large statistics, the inclusive x_π fits yield the final calibration constants (relative to the muon calibration) as a function of momentum which are used in the later fits to the x_π distributions for all the exclusive modes. For the whole momentum range, the obtained values $\bar{x}_\pi = -0.021 \pm 0.004$ and $\sigma_{x_\pi} = 0.992 \pm 0.003$ are significantly different from those (with similar errors) from the $\tau \to \mu$ sample which covers the same momentum range. These shifts are consistent with those found using a 99.5% pure pion data sample in the $h^-\pi^0$ mode by requiring the invariant mass $M(K^-\pi^0) \geq 1.1$ GeV/c^2, in order to veto the $K^*(892)^-$ background. The values $\bar{x}_\pi = -0.02 \pm 0.01$ and $\bar{\sigma}_\pi = 0.98 \pm 0.02$ are obtained in this case. A natural explanation for these shifts lies in the fact that hadrons can interact in the tracking detectors, thus producing extra tracks. Even though hemispheres with only one reconstructed track are selected, there is a residual contamination from interactions where some activity is found in the TPC around the selected track. This effect, not present with muons, modifies very slightly the calibration parameters for hadrons which are well determined from the hadron inclusive fit and verified in the simpler situation of a pure pion sample. The trend of the effect was also verified when the criteria for no-interaction were relaxed,
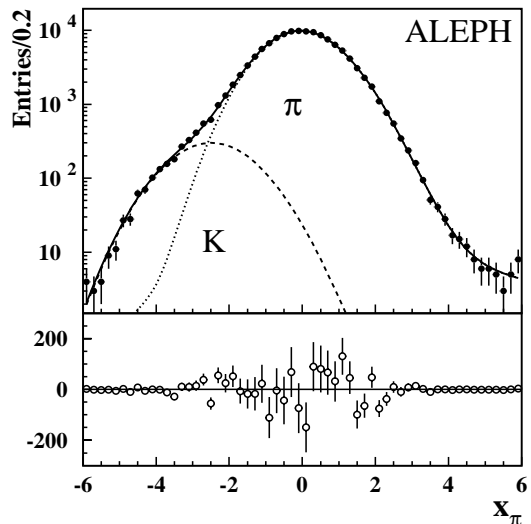
Fig. 4. Fitted x_π distribution for the inclusive one-prong hadronic τ decay sample (top). The dots with error bars correspond to data. The fit, the expected pion (including the small background from electrons and muons) and kaon contributions are indicated by the solid, dotted and dashed curves, respectively. The goodness-of-fit for the overall x_π distribution is $\chi^2/ndf = 63/57$. The residuals between the data and the fit are also shown in the bottom plot

giving confidence that the explanation had been correctly identified.

In estimating the efficiency for the inclusive mode, relative contributions from all exclusive decay modes are fixed in the Monte Carlo simulation with the exclusive branching ratios obtained later in this analysis, giving an efficiency value of $(64.05 \pm 0.03)\%$. The branching ratio for the inclusive mode is therefore obtained,

$$B(\tau^- \to K^- X \nu_\tau) = (1.52 \pm 0.04_{stat})\%, \qquad (7)$$

where X represents any system of neutral particles (including K_S^0's).

6.2 Selection for the K_L^0-reduced and K_L^0-enriched samples

The analysis of exclusive modes involving kaons divides the one-prong τ decays into K_L^0-reduced and K_L^0-enriched samples, by using cuts on the two variables $\delta\phi$ and δ_E. In the K_L^0-enriched samples, the net energy deposited in the ECAL should be at most a factor of two larger than in the HCAL, to remove the background hemispheres with unreconstructed π^0's. Meanwhile, the requirements of $\delta\phi < 0$, $\delta_E \geq 1.0$ and $\delta\phi^2 + \delta_E^2 \geq 12$ are placed on the events to reduce the non-K_L^0 background. Also, $K^-K^0\pi^0(\pi^0)$ candidates should be consistent with τ decay, *i.e.*, $M(K^-\pi^0)$ in $K^-K^0\pi^0\nu_\tau$ or $M(K^-\pi^0\pi^0)$ in $K^-K^0\pi^0\pi^0\nu_\tau$ less than $(M_\tau - M_{K^0})$. To further suppress the charged pion background from the $\pi^-\pi^0(\pi^0)$ modes, the angle α_{open} between the direction pointing from the interaction point

Table 1. Charged kaon momentum range, the fitted $x_\pi(\pi)$ parameters and kaon fractions, kaon yields, estimated non-τ background together with the test of goodness of fit. The errors in parentheses are those without the contribution from the uncertainties on the $x_\pi(\pi)$ parameters

p (GeV/c)	$\bar{x}_\pi(\pi)$	$\sigma_\pi(\pi)$	$f_K(\%)$	N_K	$N_{q\bar{q}}$	χ^2/ndf
$2.0 - 3.5$	-0.03 ± 0.01	1.00 ± 0.01	$0.11 \pm 0.12(0.11)$	10 ± 10	6 ± 2	$49.4/47$
$3.5 - 7.5$	-0.03 ± 0.01	1.00 ± 0.01	$1.30 \pm 0.11(0.10)$	320 ± 25	6 ± 2	$69.5/57$
$7.5 - 11.5$	-0.02 ± 0.01	0.99 ± 0.01	$2.82 \pm 0.15(0.14)$	625 ± 31	4 ± 2	$73.6/53$
$11.5 - 15.5$	-0.02 ± 0.01	0.99 ± 0.01	$3.92 \pm 0.23(0.20)$	680 ± 34	8 ± 2	$49.3/50$
$15.5 - 19.5$	-0.03 ± 0.01	0.98 ± 0.01	$4.59 \pm 0.34(0.26)$	607 ± 35	1 ± 1	$38.6/49$
$19.5 - 23.5$	-0.01 ± 0.01	0.98 ± 0.01	$4.83 \pm 0.44(0.32)$	508 ± 33	7 ± 2	$38.6/42$
$23.5 - 27.5$	-0.03 ± 0.01	1.01 ± 0.01	$3.48 \pm 0.50(0.35)$	303 ± 30	5 ± 2	$63.7/45$
$27.5 - 31.5$	-0.02 ± 0.02	0.99 ± 0.01	$4.17 \pm 0.58(0.39)$	303 ± 29	5 ± 2	$46.3/39$
$31.5 - 35.5$	-0.02 ± 0.02	0.98 ± 0.02	$4.30 \pm 0.69(0.46)$	247 ± 27	7 ± 2	$42.5/38$
$35.5 - 39.5$	-0.02 ± 0.02	0.98 ± 0.02	$4.35 \pm 0.99(0.60)$	199 ± 28	5 ± 2	$38.5/36$
≥ 39.5	-0.02 ± 0.02	0.98 ± 0.02	$5.04 \pm 1.21(0.70)$	204 ± 28	16 ± 3	$53.4/39$
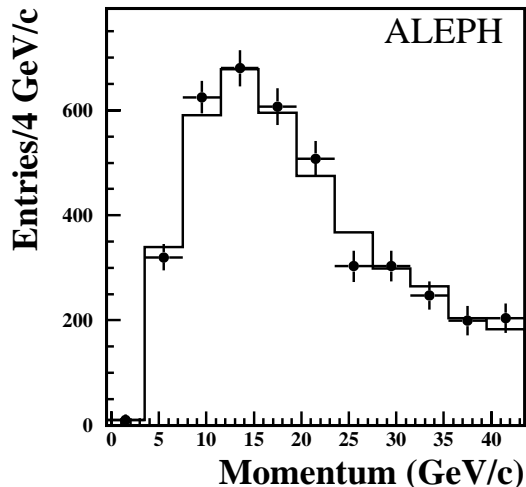
Fig. 5. The distribution of charged kaon momenta in the inclusive one-prong τ decay. The dots with error bars correspond to the fitted data and the histogram is for the Monte Carlo simulation. Errors are statistical only

to the energy-weighted barycentre in the HCAL and the $\pi^0(\pi^0)$ momentum vector, is required to be smaller than $6°$ in selecting the $K^- K^0 \pi^0(\pi^0)$ candidates. Finally, the $K^- K^0 \pi^0 \pi^0$ candidates are required to have $M(\pi^0 \pi^0)$ greater than 0.5 GeV/c^2, to reduce the $K^- K^0 \pi^0$ contamination due to the decay $K^0 \to \pi^0 \pi^0$.

The above selection criteria define the K^0_L-enriched samples for $K^- K^0$, $K^- K^0 \pi^0$ and $K^- K^0 \pi^0 \pi^0$ in the h^-, $h^- \pi^0$ and $h^- \pi^0 \pi^0$ modes. The K^0_L-reduced samples, involving decay modes like K^-, $K^- \pi^0$ and $K^- \pi^0 \pi^0$, are defined as those which do not satisfy these criteria. Finally, the kaon fraction for each sample is determined from the fit to the corresponding x_π distribution.

6.3 Charged kaon fractions in the K^0_L-reduced samples

The K^0_L-reduced samples h^-, $h^- \pi^0$ and $h^- \pi^0 \pi^0$ are used to measure the branching ratios for $K^- \nu_\tau$, $K^- \pi^0 \nu_\tau$ and $K^- \pi^0 \pi^0 \nu_\tau$. Fits to the x_π distributions (Fig. 6) are performed in each momentum bin, in order to reduce uncertainties from dynamics in the simulation. The $x_\pi(\pi)$ parameters in each momentum bin are directly taken from the values obtained in the fits to the inclusive mode as given in Table 1. Tiny fractions of muon and electron backgrounds are directly estimated from Monte Carlo and fixed in the fits. Table 2 gives the results of the fits. Figure 7 shows the charged kaon momentum distributions for both data and Monte Carlo simulations using the branching ratios obtained later. Good agreement is observed.

For the $h^- \pi^0 \pi^0 \pi^0$ mode, no cut is applied on the calorimetric measurement, and the kaon momentum is required to be greater than 5 GeV/c, reducing the pion background. The fit is only done for the whole momentum region because of low statistics. A generator with a $V - A$ matrix element and τ phase space factor is used to produce Monte Carlo events for the decay $\tau^- \to K^- \pi^0 \pi^0 \pi^0 \nu_\tau$, giving an estimate of the average K/π separation. A fit to the corresponding x_π distribution is performed, and the result is given in Table 2. Figure 6d shows the x_π distributions and the corresponding fits in the $K^- \pi^0 \pi^0 \pi^0$ mode.

6.4 Charged kaon fractions in the K^0_L-enriched samples

Decay modes such as $K^- K^0$, $K^- K^0 \pi^0$ and $K^- K^0 \pi^0 \pi^0$ are measured by fitting the x_π distributions in the K^0_L-enriched samples.

In the analysis of $h^- K^0$ mode, the fits to the x_π distributions in the K^0_L-enriched sample are also performed in momentum bins. This sample contains the tracks going through the ECAL cracks in order to enhance the selection

Table 2. Summary of statistics, overall charged kaon fractions in the x_π fit, the test of goodness-of-fit for the overall x_π distribution in each mode, estimated $q\bar{q}$ backgrounds, and the branching ratios obtained later. Errors are statistical only
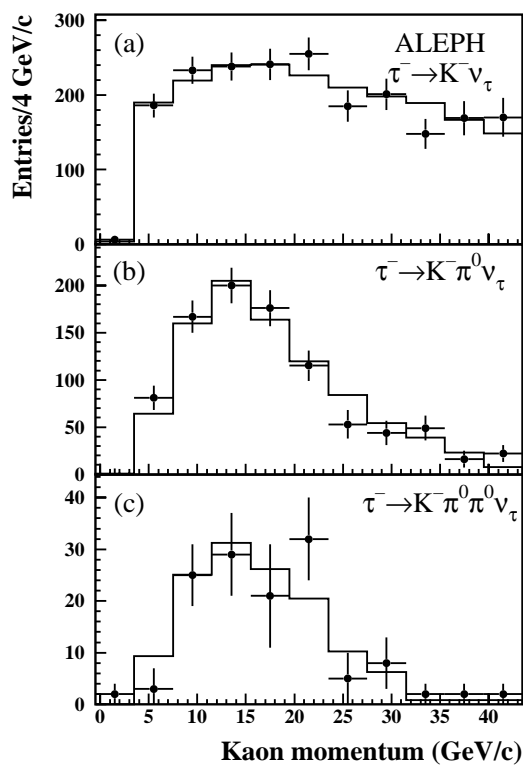
Mode	$f_K(\%)$	N_K	χ^2/ndf	$N_{q\bar{q}}$	$B(10^{-3})$
K^-	5.75 ± 0.19	2032 ± 66	$71.9/57$	11 ± 4	6.96 ± 0.25
$K^-\pi^0$	1.92 ± 0.10	923 ± 47	$68.3/57$	15 ± 5	4.44 ± 0.26
$K^-\pi^0\pi^0$	1.55 ± 0.23	131 ± 19	$52.0/47$	3 ± 1	0.56 ± 0.20
$K^-\pi^0\pi^0\pi^0$	3.43 ± 1.09	22 ± 7	$33.5/35$	< 1	0.37 ± 0.21
K^-K^0	9.20 ± 0.96	150 ± 14	$27.2/27$	2 ± 1	1.62 ± 0.21
$K^-K^0\pi^0$	9.23 ± 1.18	78 ± 10	$19.7/20$	1 ± 1	1.43 ± 0.25
$K^-K^0\pi^0\pi^0$	8.89 ± 4.44	4 ± 2	$3.2/6$	< 1	< 0.18 (95% C.L.)
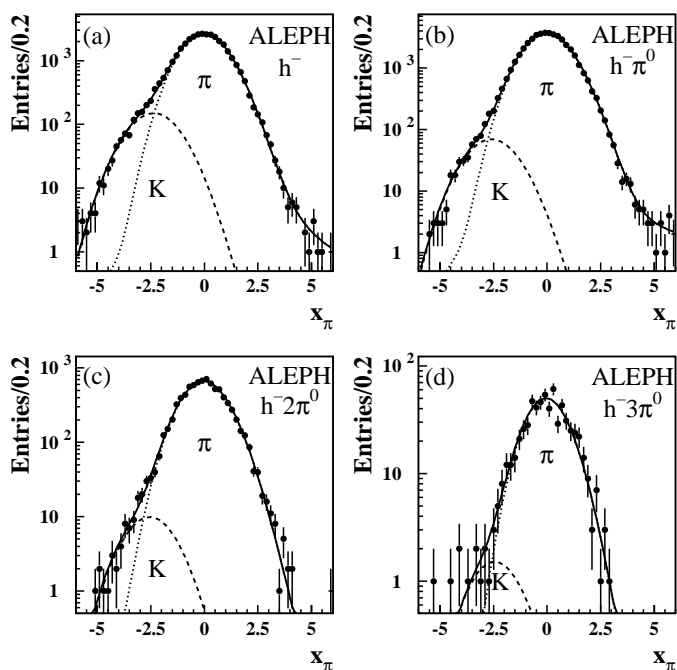
Fig. 6a–d. The x_π distributions in the K^0_L-reduced samples. Data are shown with error bars. The fit results are shown as solid curves; the kaon and pion components are given by the dashed and dotted curves, respectively; the small electron and muon contributions are included in the pion component

Fig. 7a–c. Kaon momentum distributions for the K^0_L-reduced samples: **a** h^- mode; **b** $h^-\pi^0$ mode; **c** $h^-\pi^0\pi^0$ mode. Data and Monte Carlo simulations are shown in dots with errors and in histograms, respectively. Errors on the measured kaon yields are statistical only

efficiency, consequently introducing some electron background which is taken into account in the fits and has no influence on the kaon content. The fitting procedure is the same as used above, yielding the results shown in Table 2 and Fig. 8. The charged kaon momentum distribution in the h^-K^0 mode is also shown in Fig. 9, indicating a good agreement between data and the Monte Carlo simulation.

Fits to the full momentum range are applied for the $h^-K^0\pi^0$ and $h^-K^0\pi^0\pi^0$ modes because of low statistics. To reduce the pion background, an additional 5 GeV/c cut is employed for the minimum kaon momentum. The
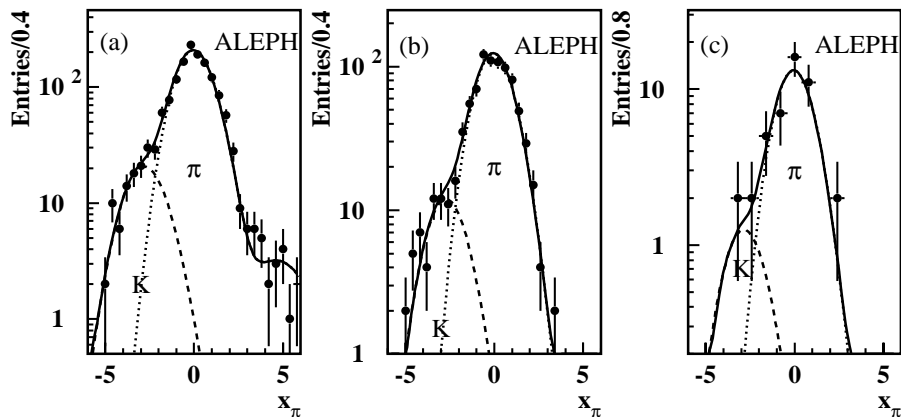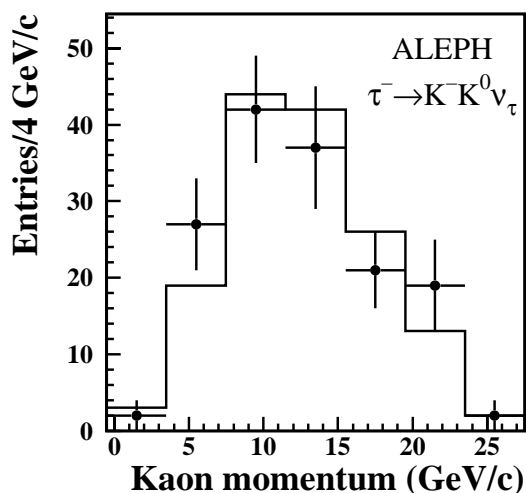
average K/π separation is obtained from the simulations. Table 2 and Fig. 8 show the results of the fits.

6.5 Branching ratios for decays with charged kaons

The measurement of the kaon yields for all exclusive modes is used to determine the corresponding branching ratios after applying the efficiency matrix obtained from Monte

Fig. 8a–c. Fitted x_π distributions in the K_L^0-enriched samples: **a** for $h^- K^0$, **b** for $h^- K^0 \pi^0$ and **c** for $h^- K^0 2\pi^0$. The dots with error bars correspond to data. The fit function and the pion (including the small electron and muon background) and kaon contributions are shown in solid, dotted and dashed, respectively

Fig. 9. Charged kaon momentum distributions for data (dots with error bars) and the expected signal from simulation (histogram)

7 Channels involving K_L^0 only

This section studies the $\overline{K^0}\pi^-$, $\overline{K^0}\pi^-\pi^0$ and $\overline{K^0}\pi^-\pi^0\pi^0$ decay modes, in which the potentially large backgrounds expected from the decay channels $\pi^-\nu_\tau$, $\pi^-\pi^0\nu_\tau$ and $\pi^-\pi^0\pi^0\nu_\tau$ are separated by means of a fit method based on the previously defined variables δ_E and $\delta\phi$.

7.1 Selection for the K_L^0 samples

In general, non-K_L^0 background can mimic a K_L^0 signal through (i) h^- with upward fluctuation of calorimetric energy; (ii) π^0 leakage into the HCAL and (iii) unreconstructed π^0's in the ECAL. As done in selecting the K_L^0-enriched samples for the purpose of measuring the charged kaons, the selection criteria are based on the measurements from both the HCAL and the ECAL. The K_L^0 candidates are required to have at least 5 GeV energy deposited in the HCAL, to remove the background from a high energy π^0 leakage. The net energy deposited in the ECAL must be smaller than 15 GeV and less than two times the energy deposited in the HCAL, rejecting background with unreconstructed π^0's. Figure 10 illustrates the power of the latter cut in a (δ_E, $\delta\phi$) region where the K_L^0 signal is dominant: the efficiency for the signal is 0.95, while the π^0 background is reduced by a factor of two. According to the Monte Carlo study, the $\pi^-\pi^0$ or $\pi^-\pi^0\pi^0$ backgrounds may produce a fake K_L^0 signal in the HCAL when part of the shower coming from a π^0 leaks into the HCAL through the cracks between ECAL modules. To remove this background a quantity ϕ_{module}, defined as the azimuthal angle for the energy-weighted barycentre in the HCAL, is required to be outside a $5°$ window centred on each ECAL crack. A further suppression of this background is achieved by requiring that δ_E be larger than 1 for $\overline{K^0}\pi^-$ and 1.5 for $\overline{K^0}\pi^-\pi^0(\pi^0)$, at the cost of a few percent signal loss. The charged hadron momentum is required to be less than 30 GeV/c for $K^0\pi^-$, 25 GeV/c for $\overline{K^0}\pi^-\pi^0$ and 20 GeV/c for $\overline{K^0}\pi^-\pi^0\pi^0$. To be consistent with τ decay, the $\overline{K^0}\pi^-\pi^0$ or $\overline{K^0}\pi^-\pi^0\pi^0$ candidates must satisfy $M(\pi^-\pi^0)$ or $M(\pi^-\pi^0\pi^0)$ less than $(M_\tau - M_{K^0})$. The angle α_{open} defined in Sect. 6.2 is required to be smaller than $8°$ for the $\overline{K^0}\pi^-\pi^0$ mode and $5°$

Carlo (see Table 3). In the simulation, form factors for the two- and three-meson decay channels are derived from [10, 11], and the four-meson τ decay channels, for which no model is available at present, are generated according to the general $V - A$ weak matrix element folded with phase space distributions for hadrons.

All channels studied in this analysis are correlated through π^0 reconstruction and K^0 contamination. Their branching ratios should thus be computed globally, by solving the seven linear equations with the efficiency matrix given in Table 3, in order to take the correlations properly into account. Since the channel $K^-\eta\nu_\tau$ can also feed into each studied mode, the corresponding subtraction is performed using the measurement $B(\tau^- \to K^-\eta\nu_\tau) = (2.9^{+1.5}_{-1.4}) \times 10^{-3}$ from ALEPH [12]. The final branching ratios for one-prong τ decays involving charged kaons are given in Table 2.

Table 3. Efficiency matrix (in percent) for the exclusive τ decay modes involving charged kaons. The K_L^0-reduced samples involve the first four decay modes, while the K_L^0-enriched samples include the last three. The generated decay modes are given in the first row, and the reconstructed modes in the first column

Mode	K^-	$K^-\pi^0$	$K^-\pi^0\pi^0$	$K^-\pi^0\pi^0\pi^0$	K^-K^0	$K^-K^0\pi^0$	$K^-K^0\pi^0\pi^0$	$K^-\eta$
K^-	65.37	4.25	0.34	~ 0	15.24	1.28	0.14	0.28
$K^-\pi^0$	0.42	44.26	7.41	1.18	4.69	8.89	2.86	1.84
$K^-\pi^0\pi^0$	~ 0	0.50	23.32	12.40	2.90	3.69	6.30	5.34
$K^-\pi^0\pi^0\pi^0$	~ 0	~ 0	0.28	8.10	~ 0	1.26	2.82	1.82
K^-K^0	0.55	0.66	~ 0	~ 0	16.86	1.82	0.48	0.26
$K^-K^0\pi^0$	~ 0	0.48	0.63	~ 0	1.32	10.04	3.74	0.20
$K^-K^0\pi^0\pi^0$	~ 0	~ 0	~ 0	0.42	~ 0	0.62	4.54	0.24
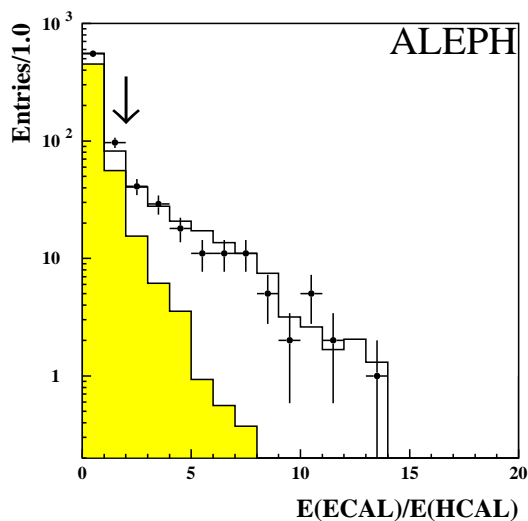
Fig. 10. The distribution of the ratio of the ECAL energy over the HCAL energy for the h topology in the K_L^0-signal dominating region with $\delta_E > 1$, $\delta\phi < 0$ and $\xi > 5$ using the variable defined in Sect. 7.2. The shaded histogram shows the distribution from the $K_L^0(K_L^0)h$ signal in the simulation and the full histogram compared to data corresponds to the sum of the signal and the background $h(\pi^0)$. The arrow indicates the location of the cut

for the $\overline{K^0}\pi^-\pi^0\pi^0$ mode. The above cuts select three samples for the study of the $\overline{K^0}\pi^-$, $\overline{K^0}\pi^-\pi^0$ and $\overline{K^0}\pi^-\pi^0\pi^0$ modes.

7.2 Measured K_L^0 fractions

The two variables δ_E and $\delta\phi$ are used to distinguish the K_L^0 events from the background. In previous analyses [3, 4], the K_L^0 signals are selected with cuts on δ_E and $\delta\phi$, while in this analysis a fit method is applied. It is observed that systematic effects from the dynamics are reduced, and at the same time the distributions of δ_E and $\delta\phi$ in data and in the simulation can be compared, providing a way to estimate the systematic uncertainties. Rather than

performing a two-dimensional fit, a one-dimensional fit is exploited using the variable ξ

$$\xi = -\frac{\sqrt{2}}{2}(\delta_E - \Delta + \delta\phi)(\text{for } \delta_E > 0, \ \delta\phi > 0), \quad (8)$$

and

$$\xi = \frac{\sqrt{2}}{2}(\delta_E - \Delta - \delta\phi)(\text{for } \delta_E > 0, \ \delta\phi \leq 0), \quad (9)$$

where Δ represents the δ_E cut used for selecting the K_L^0 sample. This procedure is equivalent to projecting each event onto one of the two ξ axes shown in Fig. 11 together with scatter plots for data and Monte Carlo. Large $\delta\phi$ and δ_E offsets are observed for the $\overline{K^0}\pi^-(K^0)$ events, while they are relatively smaller in the $K^-K^0(\pi^0)$ sample, because of the harder charged kaon momentum. The $h^-(\pi^0)$ backgrounds contribute to the K_L^0-enriched sample because of an upward energy fluctuation, yielding a long tail in the δ_E distribution. The definition of ξ is optimized for the $\overline{K^0}\pi^-(K^0)$ signal. Events with a positive (negative) sign of $\delta\phi$ always correspond to a negative (positive) sign of ξ. As a result, the majority of K_L^0's are distributed in the region of large positive ξ and are thus efficiently separated from the non-K_L^0 background.

To measure the K_L^0 fractions, the shapes of ξ distributions for both the K_L^0 modes and the non-K_L^0 modes are parametrized from the Monte Carlo simulation, using a set of Gaussian functions. Since the majority of K_L^0 events are on the positive ξ side, the negative ξ distribution can be used to check the calorimetric calibration and the simulation as well.

In the fits to the ξ distributions, the means and the widths of all the Gaussian functions for the non-K_L^0 modes are left free in order to check the simulation and the calibration. The channels involving a $K^-K_L^0$ pair are also taken into account by incorporating the shapes from the simulation and fixing the fractions from the independent measurements of the branching ratios given in Table 2. The channels involving two neutral kaons cannot be separated from those involving a single neutral kaon because the two K_L^0 showers overlap in the calorimeters. A small difference is indeed observed in the simulated ξ shapes, but the fit is not sensitive to this effect. Table 4 gives the
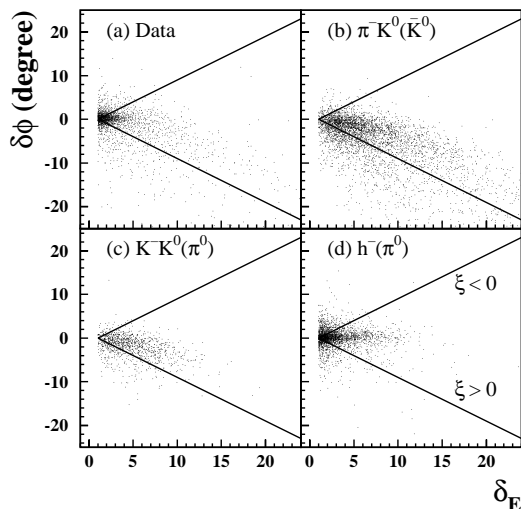
Fig. 11a–d. The scatter plots (δ_E vs $\delta\phi$) in h mode for **a** data, **b** Monte Carlo events for $\tau^- \to \overline{K^0}\pi^-(K^0)\nu_\tau$ (~5× statistics of data), **c** Monte Carlo events for $\tau^- \to K^- K^0(\pi^0)\nu_\tau$ (~ 8× data), and **d** $\tau^- \to h^-(\pi^0)\nu_\tau$ (~ 5× data). The two ξ axes considered in the analysis are drawn with straight lines as shown in each plot

Fig. 12a–c. The ξ distributions for the K_L^0 sample **a** in h^- mode; **b** in $h^-\pi^0$ mode; **c** in $h^-\pi^0\pi^0$ mode. Data are given with error bars. For $\xi > 20$, the bin width is increased to 2.0. The fits, signals ($h^- = \pi^-$) and τ backgrounds are shown as solid, dashed and dotted curves, respectively. Even though the distributions for positive and negative ξ are disconnected and vanish at $\xi = 0$ by construction apart from binning effects, it is convenient to display the overall distribution in the same histogram
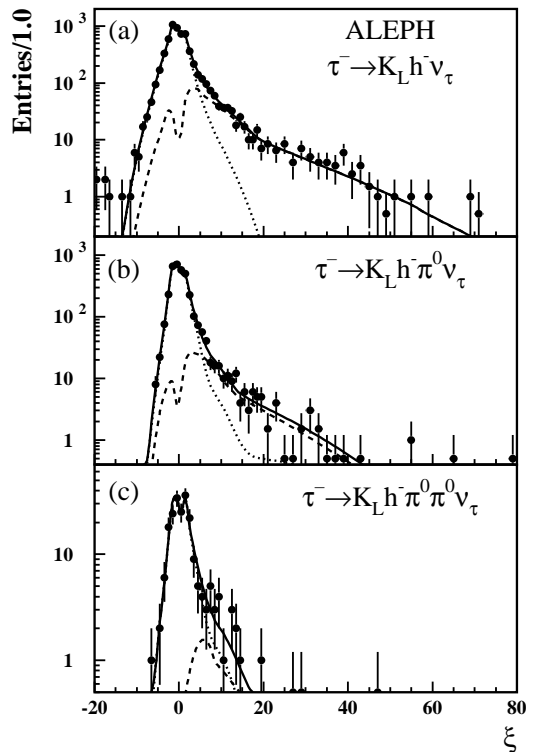
Table 4. Results from the fits to ξ distributions. The ξ parameters for the non-K_L^0 modes, the fraction of K_L^0, the corresponding number of K_L^0's, the test of goodness-of-fit in each mode, the estimated backgrounds from $K^0\overline{K^0}\pi^-\pi^0$ and $q\bar{q}$, and the branching ratios obtained later

Mode	$K_L^0\pi^-$	$K_L^0\pi^-\pi^0$	$K_L^0\pi^-\pi^0\pi^0$
$\bar{\xi}$ (non-K_L^0)	-0.04 ± 0.03	0.00 ± 0.03	-0.03 ± 0.16
$\bar{\sigma}_\xi$ (non-K_L^0)	0.98 ± 0.02	0.96 ± 0.02	1.00 ± 0.08
$f_{K_L^0}$ (%)	15.24 ± 0.68	8.67 ± 0.76	8.12 ± 3.41
$N_{K_L^0}$	937 ± 41	299 ± 26	17 ± 7
χ^2/ndf	$72.5/69$	$46.0/41$	$14.0/21$
$N(K^0\overline{K^0}\pi^-\pi^0)$	2 ± 1	16 ± 6	6 ± 2
$N_{q\bar{q}}$	25 ± 4	12 ± 3	< 1
B (10^{-3})	9.28 ± 0.45	3.47 ± 0.53	< 0.66 (95%C.L.)

results obtained in the ξ fits. Figure 12 shows all the ξ distributions and the corresponding fits to the three K_L^0-enriched samples.

7.3 Branching ratios for decays with one K^0 only

The relevant branching ratios are obtained from the measured K_L^0 yields using the efficiency matrix given in Table 5. Since the $K^0\overline{K^0}\pi^-(\pi^0)\nu_\tau$ channels can feed into the channels with a single neutral kaon, the subtraction of these backgrounds is necessary. The contribution of the $K_L^0 K_L^0\pi^-$ mode is computed using the measurement of the $K_S^0 K_S^0\pi^-\nu_\tau$ channel, assuming CP invariance. The

latest measurements [2,13] of the $K_S^0 K_S^0\pi^-$ mode give an average $(0.24 \pm 0.05) \times 10^{-3}$, significantly smaller than the value $(0.75 \pm 0.38) \times 10^{-3}$ [14] used in the previous ALEPH analyses [3,4], which relied on the assumption $B(\tau^- \to K_L^0 K_L^0\pi^-\nu_\tau)/B(\tau^- \to K^0\overline{K^0}\pi^-\nu_\tau) = 1/4$. After correcting for this effect, the published measurements [3,4] are in good agreement with the value obtained in the present analysis. Since the $K_S^0 K_L^0\pi^-$ mode can also give a contribution to all the final states as shown in Table 3, the subtraction is performed using the branching ratio $B(\tau^- \to K_S^0 K_L^0\pi^-\nu_\tau) = (1.01 \pm 0.26) \times 10^{-3}$ given by ALEPH [2]. As for the decay mode $K^0\overline{K^0}\pi^-\pi^0$, a first measurement of the branching ratio of $(0.31 \pm 0.12) \times 10^{-3}$ for the $K_S^0 K_L^0\pi^-\pi^0$ part has been obtained by ALEPH [2]. For this mode, the ratios $K_S^0 K_S^0 : K_L^0 K_L^0 : K_L^0 K_S^0$ of $1/4 : 1/4 : 1/2$ are assumed, yielding the relevant contribution to each final state given in Table 4. Finally, the branching ratios are computed using the efficiencies given in Table 5 and the numbers of neutral kaons, after doing the $K^0\overline{K^0}\pi^-\pi^0$ and $q\bar{q}$ background subtraction, where the branching ratios for K^0 are given by assuming equal K_S^0 and K_L^0 contributions. The results are given in Table 4.

Table 5. Efficiency matrix (in percent) for the exclusive τ decay modes involving one neutral kaon only. The feedthrough backgrounds from the channels involving two neutral kaons are taken into account, as detailed in the text. The generated decay modes are given in the first row, and the reconstructed mode in the first column

Mode	$K_L^0\pi^-$	$K_L^0\pi^-\pi^0$	$K_L^0\pi^-\pi^0\pi^0$	$K_L^0 K_L^0\pi^-$	$K_S^0 K_L^0\pi^-$
$K_L^0\pi^-$	45.03	4.20	0.23	32.11	3.86
$K_L^0\pi^-\pi^0$	2.34	24.42	1.17	8.71	2.93
$K_L^0\pi^-\pi^0\pi^0$	0.24	1.16	8.64	0.53	3.46

Table 6. Summary of systematic uncertainties (relative in percent). See text for details

Source	Sel	dE/dx	Calori	Bkg	MC stat	Dynam	Total
K^-X	0.3	2.6	-	0.7	0.4	0	2.7
K^-	0.4	1.6	-	0.9	0.6	0	2.0
$K^-\pi^0$	0.7	4.8	-	2.0	1.2	0	5.4
$K^-2\pi^0$	4.1	12.1	-	23.5	2.3	5.8	27.5
$K^-3\pi^0$	15.8	4.1	-	22.1	4.8	10.0	29.6
K^-K^0	0.6	1.4	3.2	1.8	2.7	5.0	6.9
$K^-K^0\pi^0$	0.9	3.4	4.2	6.9	4.2	4.0	10.5
$\overline{K^0}\pi^-$	0.6	-	2.5	2.2	1.4	0	3.7
$\overline{K^0}\pi^-\pi^0$	1.1	-	5.4	6.1	3.4	6.0	10.8

8 Systematic uncertainties

The sources of systematic uncertainties in this analysis are divided into several parts: general selection criteria, dE/dx response, calorimetric measurements, feedthrough background, Monte Carlo statistics and decay dynamics. The estimates are given in Table 6 and are detailed below.

8.1 Selection efficiency

In this analysis, one-prong τ decays are classified into h^-, $h^-\pi^0$, $h^-\pi^0\pi^0$ and $h^-\pi^0\pi^0\pi^0$ samples. The uncertainties on the selection efficiencies, studied in [4], correspond to the general τ-pair selection, the lepton/hadron separation, the γ/π^0 recognition, the handling of fake photons and the hadronic interactions. In the general τ-pair selection, a 0.2% uncertainty is given for all non-K^0 channels, while a 0.3% uncertainty is assigned to the channels involving K^0. An uncertainty of 0.2% on the lepton/hadron separation is estimated for all relevant channels, $i.e.$, without involving π^0's. The systematic uncertainty related to π^0 reconstruction increases with the number of π^0's involved. Errors of 0.6%, 2.6% and 15.7% are estimated for the channels involving one, two and three π^0's, respectively. Concerning fake photons, a detailed investigation was presented in [4]. It was found that there are some discrepancies between data and Monte Carlo, resulting in corrections which are included in the efficiency matrix in Table 3 and Table 5: $(-1.49 \pm 0.32)\%$ for $K^-\nu_\tau$, $(-0.58 \pm 0.40)\%$

for $K^-\pi^0\nu_\tau$, $(+4.28 \pm 3.17)\%$ for $K^-\pi^0\pi^0\nu_\tau$, $(+0.21 \pm 1.49)\%$ for $K^-\pi^0\pi^0\pi^0\nu_\tau$, $(-1.62 \pm 0.54)\%$ for $h^-K^0\nu_\tau$, $(+1.06 \pm 0.93)\%$ for $\overline{K^0}\pi^-\pi^0\nu_\tau$ and $(-0.59 \pm 0.61)\%$ for $K^-K^0\pi^0\nu_\tau$. The errors are taken as the systematic uncertainties. All the above four contributions to the general selection criteria are put together and given in Table 6.

8.2 dE/dx measurement

Three systematic effects are relevant to the dE/dx measurement. Following [1], the first part is the pion calibration. The corresponding uncertainty is estimated from the study of the inclusive mode, in which the fits to the x_π distributions give two values for the error on the kaon fractions (see Table 1), the first obtained from the three-parameter fits by leaving the $x_\pi(\pi)$ parameters free and the second from the one-parameter fit when fixing the $x_\pi(\pi)$ parameters. The pion calibration uncertainty is obtained from their quadratic difference, giving a 0.07% uncertainty on the absolute kaon fraction. This value is applied in a relative way to all channels involving charged kaons, yielding 2.3% (K^-X), 1.4% (K^-), 4.3% ($K^-\pi^0$), 11.1% ($K^-\pi^0\pi^0$), 3.2% ($K^-\pi^0\pi^0\pi^0$), 0.9% (K^-K^0) and 1.0% ($K^-K^0\pi^0$), respectively.

The second part is related to the shape of the pion resolution function $F_\pi(x_\pi)$ derived from the muon samples. The largest contribution to the uncertainty comes from the statistical errors in the parametrization of $F_\pi(x_\pi)$, which correspond to relative uncertainties of: 0.7% (K^-X), 0.4% (K^-), 1.2% ($K^-\pi^0$), 3.2% ($K^-\pi^0\pi^0$), 0.9% ($K^-\pi^0\pi^0\pi^0$), 0.3% (K^-K^0) and 2.9% ($K^-K^0\pi^0$), respectively. Another contribution arises from the energy dependence of the parametrization using $\tau^- \to \mu^-\bar{\nu}_\mu\nu_\tau$ and $\gamma\gamma \to \mu^+\mu^-$ events. The corresponding uncertainties are: 0.1% (K^-X), 0.1% (K^-), 0.8% ($K^-\pi^0$), 1.7% ($K^-\pi^0\pi^0$) and 0.3% (K^-K^0), respectively. The other modes with charged kaons are selected with a 5 GeV/c minimum momentum cut, thus reducing the effect studied above to a negligible level.

The third part comes from the K/π separation, which follows the calibrated velocity dependence obtained from pions. There is no additional calibration error for kaons in principle. However, for convenience the kaon resolution function, (4), is constructed from Monte Carlo tracks, hence generating small statistical uncertainties of 1.0% (K^-X), 0.8% (K^-), 1.4% ($K^-\pi^0$), 3.4% ($K^-\pi^0\pi^0$), 2.4%

$(K^-\pi^0\pi^0\pi^0)$, 1.0% (K^-K^0) and 1.4% $(K^-K^0\pi^0)$, respectively. These errors are translated into the systematic uncertainties for each channel, and finally added to the other two dE/dx uncertainties in quadrature as shown in Table 6.

8.3 Calorimetric measurements

The systematic errors due to the uncertainties in the calorimetric measurements are investigated by comparing the $\delta\phi$ and the δ_E distributions in data and Monte Carlo simulation. From the statistical errors in the calibration procedure discussed in Sect. 5.3, an uncertainty is derived, through the $\delta\phi$ cuts, on the efficiencies for the K^-K^0 and $K^-K^0\pi^-$ modes, and the feedthrough background from other τ decays, yielding systematic uncertainties of 1.0% and 1.1% the K^-K^0 and $K^-K^0\pi^-$ modes, respectively. Negligible uncertainties affect the other modes.

The precision of the δ_E measurement gives corresponding uncertainties of 2.9% (K^-K^0), 3.9% $(K^-K^0\pi^0)$, 0.2% (K^-) and 0.2% $(K^-\pi^0)$.

In selecting the K_L^0-enriched sample, a cut on the ratio of energy deposited in the ECAL and the HCAL is used to remove the background from $h^-\pi^0$ and $h^-\pi^0\pi^0$. To investigate the possible biases, two τ decay samples h^- and $3h^-$ are studied. In the h^- mode, events are required to have a positive $\delta\phi$ and a minimum 5 GeV HCAL energy. The comparison between data and Monte Carlo gives a (-2.7 ± 1.0)% correction to the efficiency estimated from the Monte Carlo simulation. In the $3h^-$ mode, a similar study is performed, yielding a (-0.2 ± 0.7)% correction. In this analysis, two hadrons are produced (charged hadron $+$ K_L^0) and an average of these two results yields (-1.5 ± 1.0)% for the $K^0h^-(\pi^0)$ modes, leading to a correction included in the efficiency matrix in Table 5.

In obtaining the ξ shape for the K_L^0 signal, an uncertainty may arise from the validity of the calibration constants obtained from the non-K_L^0 samples when applying to the K_L^0 sample with overlapping showers. To evaluate this effect, the $3h$ τ decay mode is used to mimic the K_L^0 signal: δ_E and $\delta\phi$ are computed, using only one charged track momentum but the full calorimetric measurement for the three charged hadrons. As a result, the ξ distribution looks very similar to the K_L^0 signal, providing a relevant comparison between data and Monte Carlo simulation. Applying the derived correction to the ξ fit yields a bias $\Delta f_{K_L^0} = (0.06\pm0.16)$% for the K_L^0 fraction in the $\overline{K^0}\pi^-$ mode. A relative uncertainty on the corresponding branching ratio is therefore estimated to be 1.6%. The same correction is also applied to the $\overline{K^0}\pi^-\pi^0$ mode, giving a 3.9% relative uncertainty on the branching ratio.

Finally, the systematic effect due to the calorimetric calibration is investigated. Analogous to the systematic uncertainty study for dE/dx measurement, this effect is studied by fitting the mean and the resolution of ξ (*i.e.*, three-parameter vs one-parameter fits), giving 1.6% and 3.4% relative uncertainties on the branching ratios for $\overline{K^0}\pi^-\nu_\tau$ and $\overline{K^0}\pi^-\pi^0\nu_\tau$, respectively.

8.4 Background subtraction

Since all one-prong τ decay with kaons are studied simultaneously, except for $K^-\eta$ and the modes with two neutral kaons, the uncertainties due to the feed-across effects are included in the branching ratios, taking into account the errors from the fits and the errors on the branching ratios used.

Background from ρ and a_1 can feed into the $\overline{K^0}\pi^-$ and $\overline{K^0}\pi^-\pi^0$ modes when the π^0 leaks through an ECAL crack. The cut on ϕ_{module} is designed to remove this background (see Sect. 7.1). However, the Monte Carlo simulation produces a somewhat broader shower shape in the calorimeters, leading to an uncertainty in calculating the barycentre in HCAL. To investigate this effect, a special sample is selected by requiring ϕ_{module} to be in a 5° window centred on an ECAL crack and $\xi > 5$, enriching the background from ρ and a_1 up to 50% of the total. The comparison between data and Monte Carlo shows that this background is over-estimated by a factor of (1.2 ± 0.1) in the signal region. This correction is taken into account in obtaining the ξ shapes used in Sect. 7.2 for the $h^-\pi^0$ and $h^-\pi^0\pi^0$ modes with unreconstructed π^0's. The corresponding errors are treated as systematic uncertainties, yielding 0.7% for $\overline{K^0}\pi^-\nu_\tau$ and 1.0% for $\overline{K^0}\pi^-\pi^0\nu_\tau$.

Turning to the non-τ background, mainly $q\bar{q}$, the uncertainty arises from the dynamics of kaon production. To investigate this effect, tighter cuts are applied on the hemisphere opposite to the one studied, rejecting hemispheres with a hadronic invariant mass greater than 3.0 GeV/c^2. More than 50% of the $q\bar{q}$ background is removed at a cost of about 1.2% in efficiency. Applying these cuts to the data reduces the fitted charged kaon yield by 85 ± 15. The Monte Carlo predicts that the kaons from $q\bar{q}$ background are reduced by 40 ± 6, while those from τ decay decrease by 47 ± 3, resulting in a loss of of 87 ± 7 kaons which agrees well with data and indicates that kaon production in these very low multiplicity $q\bar{q}$ events is well simulated within a 40% uncertainty. The same uncertainty is also given to the channels with neutral kaons.

8.5 Monte Carlo statistics and dynamics

Statistical uncertainties in the determination of the efficiency matrices listed in Table 3 and Table 5 are taken into account. However, the most important source of uncertainty originates from the decay models used in the generator, affecting both the kaon and the π^0 momentum spectra. This effect may produce biases when determining the momentum-dependent K/π separation, the π^0 reconstruction efficiency and the K_L^0 identification efficiency. All of these contributions are discussed below.

For the K^-, $K^-\pi^0$ and $\overline{K^0}\pi^-$ modes, the decay dynamics is well understood, and the corresponding uncertainties are neglected. Since the inclusive K^-X mode is dominated by the well established K^- and $K^-\pi^0$ modes, and the fits to the x_π distributions are performed in momentum bins, the uncertainty due to the unknown dynamics is neglected. In the K^-K^0 and $K^-\pi^0\pi^0$ modes, the fit

to the x_π distribution is performed in momentum bins, reducing the uncertainty on the determination of K/π separation to a negligible level.

In order to estimate the effect of K_L^0 and π^0 momentum spectra, the efficiencies are studied as a function of the hadronic mass. A mass uncertainty of 100 MeV/c^2 is assigned for the modelling of the $K^- K^0$, $K^- K^0 \pi^0$, $K^- \pi^0 \pi^0$ and $\overline{K^0} \pi^- \pi^0$ decay modes. The variations in the efficiencies are taken as systematic uncertainties, yielding 5.0%, 4.0%, 5.8% and 6.0% for the above decay modes, respectively. For the $K^- \pi^0 \pi^0 \pi^0$ mode, a 10% uncertainty is assigned for the unknown dynamics.

9 Investigation of mass spectra

Mass spectra are investigated in the $K^- \pi^0$, $K^- \pi^0 \pi^0$, $K^- \pi^0 \pi^0 \pi^0$, $\overline{K^0} \pi^-$, $\overline{K^0} \pi^- \pi^0$ and $K^0 K^- \pi^0$ modes. Because of the overlap between the hadronic showers, the $K^- K^0$ mode cannot be studied. The overlapping problem also affects the investigation of the total invariant mass for $\overline{K^0} \pi^- \pi^0$ and $K^0 K^- \pi^0$. Nevertheless, the study of subsystems such as $\pi^- \pi^0$ and $K^- \pi^0$ can still provide some useful information about the relevant dynamics. A more complete assessment of the resonance structure taking into account all isospin-related channels is available [15].

9.1 Mass spectra in the decays involving one K^- only

The study of mass spectra for the $K^- \pi^0$, $K^- \pi^0 \pi^0$ and $K^- \pi^0 \pi^0 \pi^0$ decay modes is different from the conventional method, in which cuts are applied to isolate the charged kaon at a cost in efficiency. Instead, this analysis generates the mass plots by fitting the number of charged kaons from the x_π distribution in each mass slice.

Since the minimum kaon momentum in the decay $\tau^- \to K^- \pi^0 \nu_\tau$ is about 3.5 GeV/c, a cut is set for excluding the low momentum tracks in the following analysis. A one-parameter fit is performed to extract the number of charged kaons in each mass slice, giving the mass plot shown in Fig. 13, with a 14% background level from other τ decays involving charged kaons and by construction no background from pions. Except for a small excess on the high mass tail in the data which is discussed elsewhere [15], the $K^*(892)^-$ signal is well predicted by the Monte Carlo simulation, with the background mainly distributed on the low mass side.

In the $K^- \pi^0 \pi^0$ analysis, the requirement on the minimum kaon momentum is raised to 5 GeV/c. The mass spectra for the $K^- \pi^0 \pi^0$, $K^- \pi^0$, and $\pi^0 \pi^0$ systems are investigated accordingly. Figure 14 shows these mass spectra for the $K^- \pi^0 \pi^0$ mode. Many τ decay channels feed into this final state and contribute about 60% of the total. However, since most backgrounds are distributed in the region of low mass, some useful information related to the channel $\tau^- \to K^- \pi^0 \pi^0 \nu_\tau$ can still be deduced. A peak at the $K^*(892)^-$ mass confirms the expected $K^*(892)^- \pi^0$ intermediate state. In general, $K_1(1270)$ and $K_1(1400)$ can
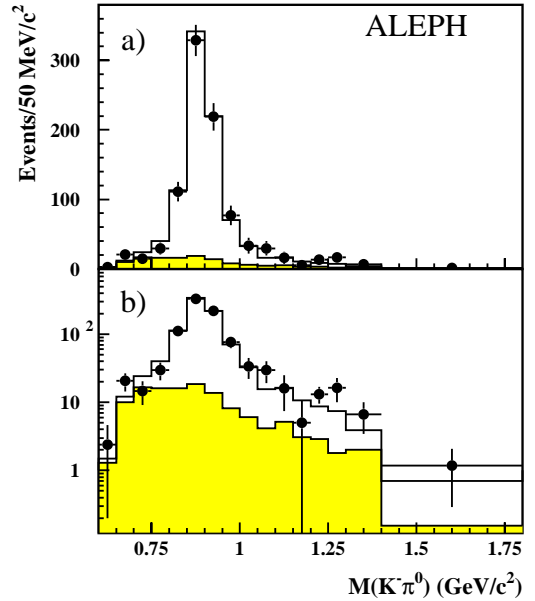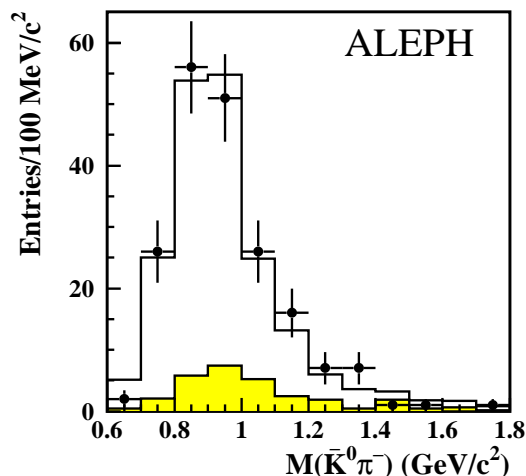

Fig. 13a,b. The $K^- \pi^0$ invariant mass spectrum for the decay channel $\tau^- \to K^- \pi^0 \nu_\tau$: **a** linear scale, **b** log scale. Data are shown as dots with error bars and the Monte Carlo predictions are shown in the open histogram together with the background distribution in shaded
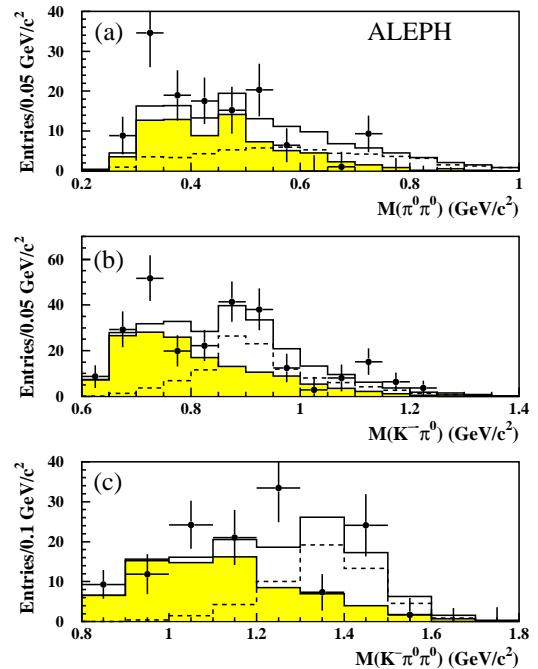

Fig. 14a–c. The invariant mass spectra for the $K^- \pi^0 \pi^0$ mode in data (dots with error bars), Monte Carlo predictions (histograms) and the expected background distribution (shaded histograms). The model predictions assuming $K_1(1400)$ dominance [10] are shown in dashed histograms
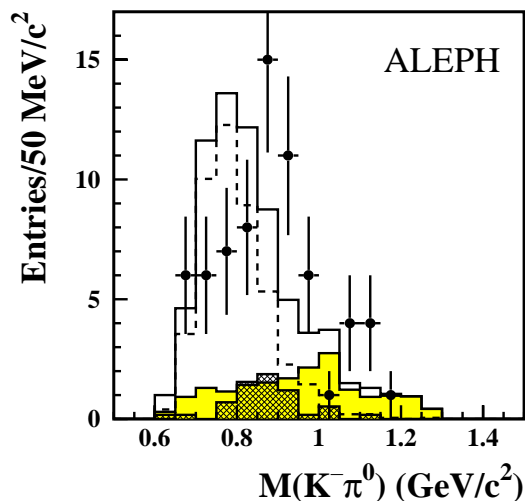
Fig. 15. The $K_L^0\pi^-$ invariant mass spectrum for the decay channel $\tau^- \to K_L^0\pi^-\nu_\tau$. Data are shown as dots with error bars. Monte Carlo predictions and the expected background distribution are shown in the open histogram and in the shaded one, respectively
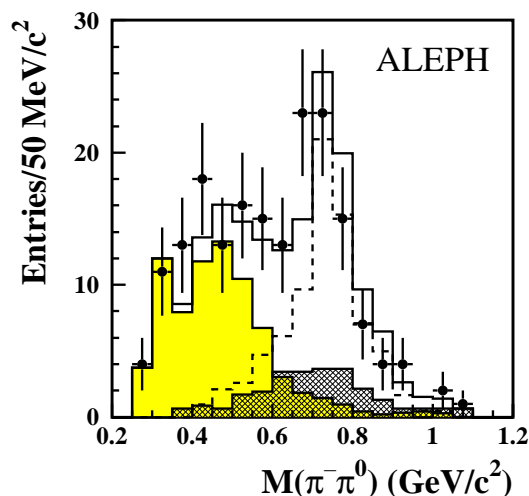
Fig. 16. The $\pi^-\pi^0$ invariant mass spectrum in the decay channel $\tau^- \to K_L^0\pi^-\pi^0\nu_\tau$. Data are shown as dots with error bars. The Monte Carlo prediction (open histogram), the background contribution from ρ^-/a_1^- (hatched histogram) and other τ backgrounds (shaded histogram) are shown, while the signal follows the dashed histogram

be produced in the $\overline{K}\pi\pi\nu_\tau$ channels. The model in [10] assumes $K_1(1400)$ dominance. However, the $K^-\pi^0\pi^0$ mass spectrum in Fig. 14 is consistent with an admixture of these two states.

Because of low statistics in the $K^-\pi^0\pi^0\pi^0$ mode, the investigation of the mass spectra is difficult. However the $\pi^0\pi^0\pi^0$ invariant mass can offer some useful information regarding the importance of the $K^-\eta$ channel. Only 5 ± 4 out of 22 ± 7 events are found in the 3π mass region (0.4–0.65 GeV/c^2), ruling out a dominant η contribution, in agreement with measurements in the $\eta \to \gamma\gamma$ mode [12].

Fig. 17. The $K^-\pi^0$ invariant mass spectrum for the $K_L^0 K^-\pi^0$ candidates. Data (dots with error bars), Monte Carlo prediction (open histogram), background contribution from $K^-\pi^0(\pi^0)$ (hatched histogram) and other τ backgrounds (shaded histogram) are shown, while the signal follows the dashed histogram

Most of the charged kaons are found in the region $M(3\pi^0)$ above 0.65 GeV/c^2, in which signal and background from $K^-K^0\pi^0\nu_\tau$ with $K_S^0 \to \pi^0\pi^0$ overlap.

9.2 Mass spectra in the decays involving one K_L^0 only

Candidates for the channels involving one K_L^0 are isolated by using cuts on both $\delta\phi$ and ξ. In the $K_L^0\pi^-$ mode, the charged pion momentum can be small, resulting in a gap between the K_L^0 and π^- showers. The requirements $\delta\phi < -10$ and $\xi \geq 10$ remove almost all non-K_L^0 background, yielding a purity of 86% for the decay channel $\tau^- \to K_L^0\pi^-\nu_\tau$. The K_L^0 flight direction is defined from the colliding point to the barycentre of the energy deposited by the K_L^0 in the HCAL. The distribution of the invariant mass $M(K_L^0\pi^-)$ is shown in Fig. 15, with a clear $K^*(892)^-$ signal seen. The backgrounds from non-K^* decay modes, such as the channels $K_L^0 K_L^0\pi^-\nu_\tau$ and $K_L^0\pi^-\pi^0\nu_\tau$, give a 10% contamination, while the $q\bar{q}$ background contributes 4%. The Monte Carlo simulation is observed to be in good agreement with data, showing that the energy measured in the HCAL is adequately simulated.

In the $K_L^0\pi^-\pi^0$ mode, the total invariant mass provides less information because of the rather poorly reconstructed K_L^0 momentum and the low statistics. However, the study of the $\pi^-\pi^0$ invariant mass distribution can give useful constraints on the relevant dynamics.

The $K_L^0\pi^-\pi^0$ candidates are selected by requiring the total measured energy in the HCAL to be greater than 10 GeV, the angle α_{open} (defined in Sect. 6.2) less than 6° and $\xi > 5$. Under these additional requirements, the backgrounds from ρ^-/a_1^-, $K^*(892)^-$, $\overline{K^0}K^0\pi^-$ and $\overline{K^0}K^0\pi^-\pi^0$ are suppressed to levels of 14%, 26%, 8% and 8%, respec-

Table 7. Summary of branching ratios obtained in this analysis. For the inclusive mode, X represents any system of neutral particles. The quoted errors are statistical and systematical, in this order

| Decay	$B \ (10^{-3})$
$\tau^- \to K^- X \nu_\tau$	$15.20 \pm 0.40 \pm 0.41$
$\tau^- \to K^- \nu_\tau$	$6.96 \pm 0.25 \pm 0.14$
$\tau^- \to K^- \pi^0 \nu_\tau$	$4.44 \pm 0.26 \pm 0.24$
$\tau^- \to K^- \pi^0 \pi^0 \nu_\tau$	$0.56 \pm 0.20 \pm 0.15$
$\tau^- \to K^- \pi^0 \pi^0 \pi^0 \nu_\tau$ (excl. η)	$0.37 \pm 0.21 \pm 0.11$
$\tau^- \to K^- K^0 \nu_\tau$	$1.62 \pm 0.21 \pm 0.11$
$\tau^- \to K^- K^0 \pi^0 \nu_\tau$	$1.43 \pm 0.25 \pm 0.15$
$\tau^- \to K^- K^0 \pi^0 \pi^0 \nu_\tau$	< 0.18 (95% C.L.)
$\tau^- \to \overline{K^0} \pi^- \nu_\tau$	$9.28 \pm 0.45 \pm 0.34$
$\tau^- \to \overline{K^0} \pi^- \pi^0 \nu_\tau$	$3.47 \pm 0.53 \pm 0.37$
$\tau^- \to \overline{K^0} \pi^- \pi^0 \pi^0 \nu_\tau$	< 0.66 (95% C.L.)

tively. The $\pi^- \pi^0$ invariant mass is shown in Fig. 16. An incoherent sum of a ρ Breit-Wigner signal and the shape of the $\overline{K}^* \pi$ reflections is used to fit to the background-subtracted $\pi^- \pi^0$ invariant mass plot, giving $(72 \pm 12 \pm 10)\%$ for the $\overline{K}\rho$ fraction, where the second 10% uncertainty is due to the background subtraction.

9.3 Mass spectra in the decays involving a $K^- K_L^0$ pair

As mentioned before, the total invariant mass distributions in $K^- K_L^0 \nu_\tau$ and $K^- K_L^0 \pi^0 \nu_\tau$ cannot be usefully studied. However, the $K^- \pi^0$ mass plot in $K^- K_L^0 \pi^0 \nu_\tau$ can be investigated. A requirement $x_\pi < -2$ is added for the $K_L^0 h^- \pi^0$ candidates, leading to a purity of 65%. The $K^- \pi^0$ mass plot is shown in Fig. 17 with a clear $K^*(892)^-$ signal observed. Although the feedthrough $K^- \pi^0 (\pi^0)$ background can fake a $K^*(892)^-$ signal, it cannot account for such an excess in the $K^*(892)^-$ mass region. In the model of [10] used in the Monte Carlo simulation, the $K^* K^0$ intermediate state in $K^- K^0 \pi^0 \nu_\tau$ is treated as strongly suppressed, which disagrees with this observation. After subtraction of the background, the $K^- \pi^0$ invariant mass distribution for the decay $\tau^- \to K^0 K^- \pi^0 \nu_\tau$ is fitted with two components, $K^* K$ and $\rho \pi$, showing that the $K^* K$ intermediate state contribution in $K^0 K^- \pi^0 \nu_\tau$ is dominant (larger than 86%). This observation is consistent with the result from the $K^+ K^- \pi^-$ mode studied in [1].

10 Results and discussion

All measured branching ratios in this analysis are listed in Table 7. The inclusive branching ratio for $\tau^- \to K^- X \nu_\tau$ is measured to be $(1.52 \pm 0.04_{stat} \pm 0.04_{sys}\%$, where X represents any system of neutral particles. The sum of all measured exclusive branching ratios gives $(1.46 \pm 0.05_{stat} \pm 0.04_{sys})\%$, in agreement with the inclusive value.
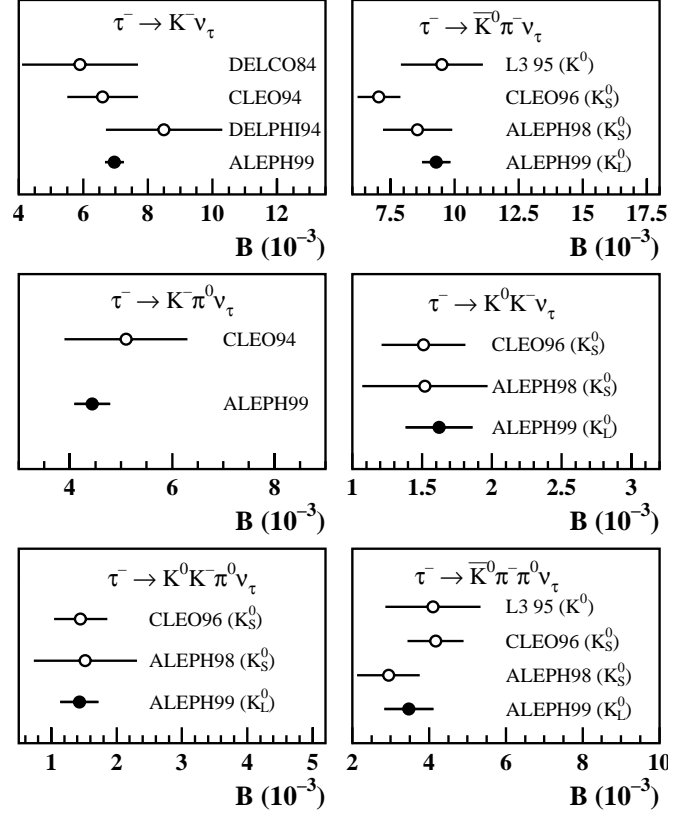
Fig. 18. The published branching ratios for one-prong τ decays with kaons [17]. The black dots correspond to this analysis. The detected K^0 modes are given in parentheses for each experiment

The $(\overline{K}\pi)^-$ mode is studied in two final states, $K^- \pi^0$ and $K_L^0 \pi^-$, both showing dominance of $K^*(892)^-$.

The measurement of τ decay into $K^- \pi^0 \pi^0 \nu_\tau$ completes the study of the $(\overline{K}\pi\pi)^-$ final states started in [1,2]. The branching ratio $B(\tau^- \to K^- \pi^0 \pi^0 \nu_\tau) = (0.56 \pm 0.20_{stat} \pm 0.15_{sys}) \times 10^{-3}$ is significantly smaller than the value (1.1–1.4) $\times 10^{-3}$ predicted in the model of [11], but in good agreement with the value 0.4×10^{-3} in [16]. This channel suffers from a large background contamination as evidenced by the study of invariant mass spectra. Despite this, a dominant $K^*(892)^- \pi^0$ intermediate state is observed. Background from $K^- \pi^0 \pi^0 \pi^0 \nu_\tau$ is found to contribute to the $K^- \pi^0 \pi^0$ mode, resulting in a difference from the previous ALEPH measurement $B(\tau^- \to K^- \pi^0 \pi^0 \nu_\tau) = (0.80 \pm 0.20_{stat} \pm 0.20_{sys}) \times 10^{-3}$ [4], wherein this background was ignored.

Assuming that the decay $\tau^- \to \overline{K^0} \pi^- \pi^0 \nu_\tau$ proceeds via incoherent intermediate states $\overline{K}\rho$ and $\overline{K}^* \pi$, one can derive the following contributions:

$$B(\tau^- \to (\overline{K}^* \pi)^- \nu_\tau \to \overline{K^0} \pi^- \pi^0 \nu_\tau)$$
$$= (0.97 \pm 0.44_{stat} \pm 0.36_{sys}) \times 10^{-3}, \quad (10)$$
$$B(\tau^- \to (\overline{K}\rho)^- \nu_\tau \to \overline{K^0} \pi^- \pi^0 \nu_\tau)$$
$$= (2.50 \pm 0.57_{stat} \pm 0.44_{sys}) \times 10^{-3}. \quad (11)$$

These results are in agreement with the measurement based on the K_S^0 mode [2].

Finally, it is found that the decay $\tau^- \to K^- K^0 \pi^0 \nu_\tau$ mainly proceeds via the $K^* K$ intermediate state.

11 Conclusion

One-prong τ decays involving either charged and/or neutral kaons are measured in this analysis. As already done in the other two ALEPH analyses [1,2], the study of final states is extended up to four hadrons involving kaons, giving a complete measurement for all sectors of τ decays involving kaons. The results are given in Table 7 and also shown in Fig. 18 to compare with other experiments [17]. Agreement is observed with all the published data. A forthcoming paper will combine all ALEPH measurements on τ decays involving kaons and will give the relevant physics implications [15].

References

1. ALEPH Collaboration, *Three-prong τ decays with charged kaons*, Eur. Phys. J. **C1** (1998) 65.
2. ALEPH Collaboration, K_S^0 *production in τ decays*, Eur. Phys. J. **C4** (1998) 29.
3. ALEPH Collaboration, *One-prong τ decays into charged kaons*, Phys. Lett. **B332** (1994) 209.
4. ALEPH Collaboration, *τ hadronic branching ratios*, Z. Phys. **C70** (1996) 579.
5. ALEPH Collaboration, K^0 *production in one-prong τ decays*, Phys. Lett. **B332** (1994) 219.
6. ALEPH Collaboration, *ALEPH: A detector for electron-positron annihilation at LEP*, Nucl. Instrum. and Methods **A294** (1990) 121; *'Performance of the ALEPH detector at LEP'*, Nucl. Instrum. and Methods **A360** (1995) 481.
7. ALEPH Collaboration, *τ leptonic branching ratios*, Z. Phys. **C70** (1996) 561.
8. KORALZ, S. Jadach, B.F.L. Ward and Z. Wąs, Comp. Phys. Commun. **66** (1991) 276; Comp. Phys. Commun. **79** (1994) 503; TAUOLA, S. Jadach, Z. Was, R. Decker and J.H. Kühn, Comp. Phys. Commun. **76** (1993) 361.
9. T. Sjöstrand, Comp. Phys. Commun. **82** (1994) 74.
10. R. Decker, E. Mirkes, R. Sauer and Z. Wąs, Z. Phys. **C58** (1993) 445.
11. M. Finkemeier and E. Mirkes, Z. Phys. **C69** (1996) 243.
12. ALEPH Collaboration, *A study of τ decays involving η and ω mesons*, Z. Phys. **C74** (1997) 263.
13. T.E. Coan et al., CLEO Collaboration, Phys. Rev. **D53** (1996) 6037.
14. M. Acciarri et al., L3 Collaboration, Phys. Lett. **B352** (1995) 487.
15. ALEPH Collaboration, *Study of τ decays involving kaons, spectral functions and determination of the strange quark mass*, CERN-EP/99-026.
16. B.A. Li, Phys. Rev. **D55** (1997) 1436.
17. R.M. Barnett et al., Particle Data Group, Eur. Phys. J. **C3** (1998) 1.